

ACCEPTED MANUSCRIPT • OPEN ACCESS

Characterisation of CVD diamond with high concentrations of nitrogen for magnetic-field sensing applications

To cite this article before publication: Andrew Mark Edmonds *et al* 2021 *Mater. Quantum. Technol.* in press <https://doi.org/10.1088/2633-4356/abd88a>

Manuscript version: Accepted Manuscript

Accepted Manuscript is “the version of the article accepted for publication including all changes made as a result of the peer review process, and which may also include the addition to the article by IOP Publishing of a header, an article ID, a cover sheet and/or an ‘Accepted Manuscript’ watermark, but excluding any other editing, typesetting or other changes made by IOP Publishing and/or its licensors”

This Accepted Manuscript is © 2020 The Author(s). Published by IOP Publishing Ltd.

As the Version of Record of this article is going to be / has been published on a gold open access basis under a CC BY 3.0 licence, this Accepted Manuscript is available for reuse under a CC BY 3.0 licence immediately.

Everyone is permitted to use all or part of the original content in this article, provided that they adhere to all the terms of the licence <https://creativecommons.org/licenses/by/3.0>

Although reasonable endeavours have been taken to obtain all necessary permissions from third parties to include their copyrighted content within this article, their full citation and copyright line may not be present in this Accepted Manuscript version. Before using any content from this article, please refer to the Version of Record on IOPscience once published for full citation and copyright details, as permissions may be required. All third party content is fully copyright protected and is not published on a gold open access basis under a CC BY licence, unless that is specifically stated in the figure caption in the Version of Record.

View the [article online](#) for updates and enhancements.

Characterisation of CVD diamond with high concentrations of nitrogen for magnetic-field sensing applications

Andrew M. Edmonds¹, Connor A. Hart², Matthew J. Turner^{2,3}, Pierre-Olivier Colard¹, Jennifer M. Schloss^{2,3}, Kevin Olsson⁴, Raisa Trubko^{2,5}, Matthew L. Markham¹, Adam Rathmill¹, Ben Horne-Smith¹, Wilbur Lew⁶, Arul Manickam⁶, Scott Bruce⁶, Peter G. Kaup⁶, Jon C. Russo⁶, Michael J. DiMario⁶, Joseph T. South⁶, Jay T. Hansen⁶, Daniel J. Twitchen¹, Ronald L. Walsworth^{2,3,4,7,8,9}

¹ Element Six Global Innovation Centre, Fermi Avenue, Harwell Oxford, Didcot, Oxfordshire OX11 0QR, UK

² Department of Physics, Harvard University, Cambridge, MA 02138, USA

³ Center for Brain Science, Harvard University, Cambridge, MA 02138, USA

⁴ Department of Electrical and Computer Engineering, University of Maryland, College Park, MD 20742, USA

⁵ Department of Earth and Planetary Sciences, Harvard University, Cambridge, MA 02138, USA

⁶ Lockheed Martin, 199 Borton Landing Road, 101-202 Moorestown, NJ 08057-0927, USA

⁷ Harvard-Smithsonian Center for Astrophysics, Cambridge, MA 02138, USA

⁸ Department of Physics, University of Maryland, College Park, MD 20742, USA

⁹ Quantum Technology Center, University of Maryland, College Park, MD 20742, USA

E-mail: andrew.edmonds@e6.com

Abstract. Ensembles of nitrogen-vacancy (NV) centres in diamond are a leading platform for practical quantum sensors. Reproducible and scalable fabrication of NV-ensembles with desired properties is crucial, as is an understanding of how those properties influence performance. This work addresses these issues by characterising nitrogen-doped diamond produced by the chemical vapour deposition (CVD) method across a range of synthesis conditions. This is shown to produce material with widely differing absorption characteristics, which is linked to the level of parasitic defects other than substitutional nitrogen (N_S) and NV. In such material, the achievable concentration of NV^- ($[NV^-]$) is found to be influenced by the as-grown properties. At the 10–20 ppm level for $[N_S]$, the production of CVD-grown material with strain levels sufficient not to limit achievable device sensitivity is demonstrated and a favourable product of $[NV^-]$ and T_2^* is obtained. Additionally, reproducible properties over a batch of 23 samples from a single synthesis run are achieved, which appears promising for the scalability efforts underway in this area of research.

Characterisation of CVD diamond for magnetic-field sensing

1. Introduction

The nitrogen-vacancy (NV) centre in diamond has been widely studied over the last decade. This is by virtue of the fact that the negative-charge state (NV^-) has a spin $S=1$ ground state that may be initialised and read-out optically [1] and coherently controlled through the application of microwaves, with the spin-state having long coherence times even at room-temperature [2, 3].

The ability to detect and control single NV^- centres was largely responsible for the initial interest in this colour centre [4] and it was established that, in addition to its potential use as a qubit or source of single-photons, diamond containing NV^- is a useful platform for the detection of electric fields, magnetic fields, temperature, and forces [5–7]. For example, magnetic-field (B) measurements may be made through probing the NV spin levels, which are split by the electronic Zeeman interaction (figure 1(a)), utilising either DC or AC-detection schemes [8]. For these single-NV demonstrations, the availability of suitable high-purity material grown by the Chemical Vapour Deposition (CVD) method was crucial [9, 10].

More recently, ensembles of NV^- centres have been demonstrated to provide routes to high-sensitivity and low-drift broadband B-field sensing, reaching picotesla (or lower) sensitivities under ambient (room temperature) conditions [11]. This is whilst providing intrinsic vector-field [12, 13] measurement capabilities through detection of all four of the NV orientations permitted by the defect's symmetry in diamond (refer to figure 1(b)). Wide-field B-field imaging using NV-ensembles [14–18] has been utilised across a spectrum of disciplines, including biology [14, 15], geophysics [18], materials science [17, 19, 20] and electronic-circuit diagnostics [21, 22]. NV-ensemble magnetometry also has potential applications in RF-sensing [23], magnetic navigation [24], magnetic-anomaly detection [25], and geo-surveying. Crucial to the success of these efforts is the availability of diamond samples offering ensembles of NV centres with reproducible properties, at a range of well-controlled concentrations appropriately chosen for each application and its practical constraints (size, weight, power, sensitivity, etc.).

1.1. Material considerations for NV magnetic field sensitivity

For NV-ensembles, the optical shot-noise limited DC magnetic sensitivity (η) is given by [26, 27]:

$$\eta \sim \frac{1}{g_e \mu_B} \frac{1}{C \sqrt{\beta}} \frac{1}{\sqrt{N_{NV} T_2^*}} \quad (1)$$

where N_{NV} is the number of NV^- centres that are utilised in the sensor (given by the product of the concentration of NV^- centres, $[NV^-]$, and the interrogated volume of the diamond), T_2^* is the ensemble spin dephasing time, β is the optical detection efficiency, and C is the measurement contrast. The physical constants g_e and μ_B are the Landé factor and Bohr magneton, respectively. Consequently, the sensitivity is both a function of the diamond material and the overall sensor design. The material-related

Characterisation of CVD diamond for magnetic-field sensing

3

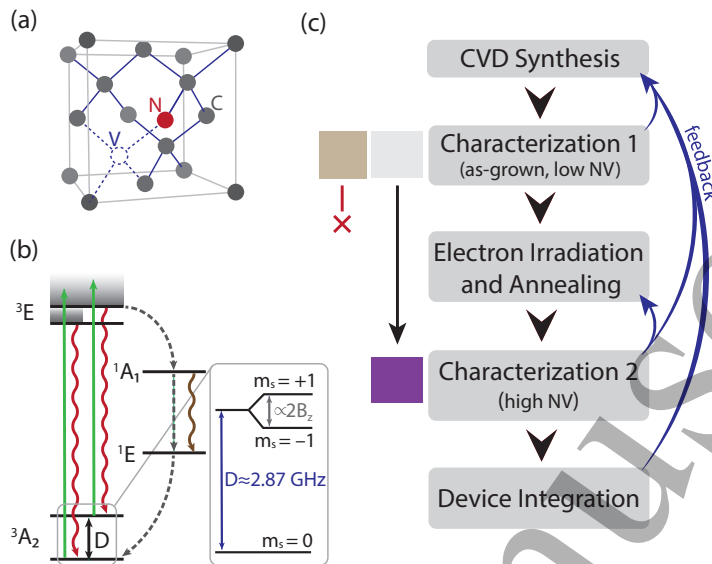


Figure 1. NV⁻ energy level and structure diagrams and material development procedure. (a) Energy level diagram for the NV⁻ centre in diamond with zero-field-splitting between ground-state electronic spin levels $m_s = 0$ and $m_s = \pm 1$. Expanded zoom depicts the Zeeman splitting of the $m_s = \pm 1$ energy levels due to an applied magnetic field B_z along the NV symmetry axis. (b) Structural diagram of the nitrogen-vacancy centre in diamond. (c) Schematic summarising the development of a process for producing diamond material for NV-ensemble magnetometry. Evolution of sample colour from a dull brown or yellow to an intense, uniform purple colour after irradiation and annealing is a result of high [NV⁻] with minimal unwanted other defects.

factors N_{NV} , C , and T_2^* have recently been the topic of an in-depth review on routes to optimise sensitivity [28], which further motivates this work.

A typical approach to create NV centres in diamond is to start with a sample produced by high-pressure high-temperature (HPHT) or CVD synthesis containing substitutional nitrogen (N_S); to electron-irradiate to create vacancies (V); and then to anneal at temperatures $> 600^\circ\text{C}$, where the V are mobile (see figure 1(c) for example images of material at different stages) [29]. The negative-charge state NV⁻, which has the physical properties utilised in sensing, arises from the donation of an electron (typically from N_S^0) according to $\text{NV}^0 + N_S^0 \rightarrow \text{NV}^- + N_S^+$. The neutral charge state NV⁰ exhibits an optical luminescence spectrum that overlaps with that of NV⁻ such that NV⁰ is the dominant contribution to background luminescence in a typical device, degrading the contrast [30, 31]. As a result, it is important to consider the concentration of both NV⁰ and NV⁻ in a sample from the perspective of increasing contrast. Therefore the fraction of NV⁻ becomes an important figure of merit:

$$\psi = \frac{[\text{NV}^-]}{[\text{NV}^-] + [\text{NV}^0]} \quad (2)$$

Factors influencing ψ include the starting level of $[N_S]$ in the diamond material, which influences the upper limit of the possible level of $[\text{NV}]$; the irradiation dose

Characterisation of CVD diamond for magnetic-field sensing

4

(i.e., [V]); and the annealing recipe used to convert N_S and V present post-irradiation into NV. Other defects, X, present in the diamond, either post-growth (CVD-specific examples are discussed in section 1.2) or post-irradiation [32], may additionally act as donors/acceptors and influence ψ .

$[NV^-]$, $[NV^0]$ and $[N_S^0]$ also influence the resulting ensemble NV dephasing time T_2^* , as they contribute to the electronic spin-bath. [X] is also a potential factor in determining T_2^* , if the defects are paramagnetic. ^{13}C has a nuclear spin of $I = \frac{1}{2}$ and therefore adds to the nuclear spin-bath. It is thus typical to produce diamond samples with depleted levels of $[^{13}C]$ in order to maximise T_2^* [2]. The final source of ensemble dephasing intrinsic to the diamond material is non-uniform strain across the area of the diamond sample being utilised [33, 34]. Considering these contributions, the material-related T_2^* can be approximated by the following expression [28, 35]:

$$\frac{1}{T_2^*(\text{material})} \approx \frac{1}{T_2^*(N_S^0)} + \frac{1}{T_2^*(NV^-)} + \frac{1}{T_2^*(NV^0)} + \frac{1}{T_2^*(X)} + \frac{1}{T_2^*(^{13}C)} + \frac{1}{T_2^*(\text{strain})} \quad (3)$$

Since the N_{NV} term in equation 1 is given by the product of $[NV^-]$ and the interrogated volume of the diamond, these two variables are important characteristics to examine. In particular, increasing $[NV^-]$ can lead to reduced T_2^* , e.g., through increased $[N_S]$ (equation 3). Thus, a critical figure of merit is the product of $[NV^-]$ and T_2^* . However, the upper-limit for $[NV]$ produced by irradiation and annealing is dictated by the starting $[N_S]$, with previous studies suggesting that $[NV]$ saturates at $[N_S]/2$ and prior to saturation all vacancies introduced by irradiation can be converted to NV [65]. Hence a key material-related decision is the as-grown $[N_S]$ and an alternative figure of merit for an as-grown material becomes the product of $[N_S^0]$ and T_2^* .

The interplay between the optimal $[NV^-]$ and T_2^* at different $[^{13}C]$, and resulting consequences for magnetic sensitivity, can therefore be informed by considering the effect of $[N_S^0]$ and $[^{13}C]$ on T_2^* . The expected T_2^* , assuming that $[N_S^0]$ and $[^{13}C]$ are the dominant contributors to the dephasing time, can be estimated using the expression:

$$\frac{1}{T_2^*(^{13}C, N_S^0)} \approx A_{^{13}C} \times [^{13}C] + A_{N_S^0} \times [N_S^0] \quad (4)$$

where, from previous measurements, $A_{^{13}C} \approx 0.100 \text{ ms}^{-1} \text{ ppm}^{-1}$ and $A_{N_S^0} \approx 101 \text{ ms}^{-1} \text{ ppm}^{-1}$ [28, 35]. The contribution from NV^- centres after irradiation and annealing is expected to be proportional to $[N_S^0]$ and is thus not explicitly included in the subsequent analysis. The contribution of other nitrogen-related, paramagnetic defects which may be present, such as NVH^- , can be treated similarly. Using equation 4, the dependence of T_2^* on $[N_S^0]$ for natural abundance ^{13}C (1.1%, 11000 ppm) and depleted ^{13}C (0.005%, 50 ppm) is illustrated in figure 2(a), including example measurements performed by our collaboration and reported in past work [28, 35].

Figure 2(b) depicts the product of $[N_S^0]$ and T_2^* for both natural abundance ^{13}C (1.1%, 11000 ppm) and isotopically depleted ^{13}C (0.005%, 50 ppm). Across the range

Characterisation of CVD diamond for magnetic-field sensing

5

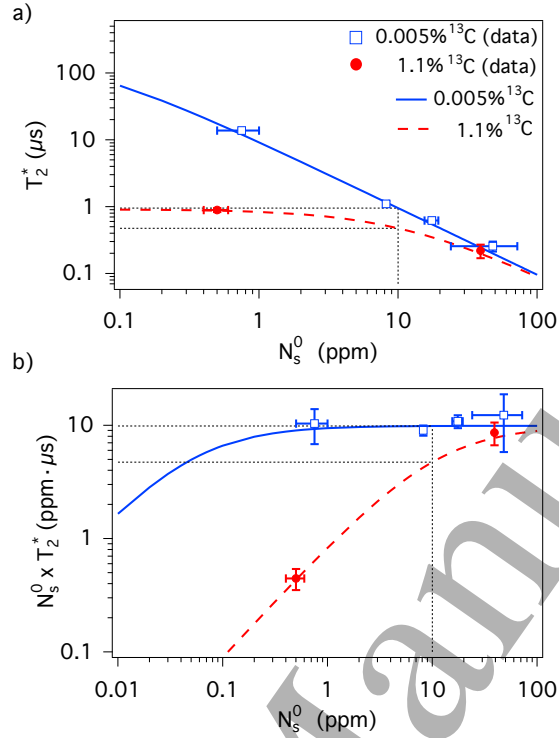


Figure 2. (a) Expected dependence of ensemble NV⁻ T_2^* with varying $[N_S^0]$ and ^{13}C , according to equation 4. (b) Product of $[N_S^0]$ and T_2^* as a function of $[N_S^0]$. The $[N_S^0] \sim 10$ –15 ppm regime, the focus of the present paper, is indicated by the dashed, black lines. Comparisons to measurements from our collaboration are shown [28, 35].

of $[N_S^0]$ depicted, the concentration of ^{13}C (^{13}C) has a critical role in determining both the achievable magnetic sensitivity and optimal $[N_S^0]$.

From figures 2(a,b) it is apparent that, for $[N_S^0]$ below ~ 100 ppm, ^{13}C -isotopic depletion is advantageous, extending T_2^* and increasing the figure of merit $[N_S^0] \times T_2^*$. Furthermore, as discussed in Barry *et al*, if nitrogen-related dephasing is a small contribution to T_2^* , then the nitrogen concentration should be increased until similar to the dominant dephasing source [28]. This is illustrated by the plateau in the product of $[N_S^0]$ and T_2^* for increasing $[N_S^0]$ in figure 2(b). While in natural abundance material $[N_S^0] \times T_2^*$ plateaus at $[N_S^0] \sim 100$ ppm, ^{13}C -depletion reduces the optimal $[N_S^0]$ to approximately 1–20 ppm.

Since the figure of merit for ^{13}C -depleted material is largely constant in the range 1–20 ppm, additional factors should be considered when choosing a target $[N_S^0]$ in this regime. For pulsed magnetometry protocols such as Ramsey, lower $[N_S^0]$ and longer T_2^* may provide advantages such as improved measurement duty cycle. However, achieving longer T_2^* in practice requires better control of other dephasing sources such as magnetic-bias-field gradients and strain inhomogeneity across an interrogated NV⁻ ensemble. Consequently, $[N_S^0]$ of order 10–15 ppm is attractive, as it relaxes these material and sensor design requirements without degrading the figure of merit $[N_S^0] \times T_2^*$.

Characterisation of CVD diamond for magnetic-field sensing

6

These considerations are especially critical when increasing the sensing volume for bulk magnetometry and wide-field magnetic field imaging applications using NV-ensembles.

1.2. Development of CVD diamond for ensemble NV magnetic-field sensors

The present work focuses on CVD diamond. Due to the morphology that evolves during growth, HPHT single-crystal diamond has different sectors present (e.g., $\{100\}$ and $\{111\}$) and the incorporation of N differs significantly between these regions [36]. Hence HPHT material must be processed into plates consisting of a single-sector, which can limit the volume of any given sensor element that can be produced. Also, it remains unclear whether controllable and reproducible levels of $[N_S]$ and hence $[NV^-]$ can be obtained in HPHT diamond. Additionally, it is not practical with the HPHT method to create diamonds with NV-ensemble surface layers for wide-field magnetic-imaging applications. Hence, at present, CVD-produced material appears to be applicable to the widest range of NV sensing modalities and applications.

Here, we investigate two potential issues for the production of diamond for NV-ensemble magnetometry applications by the CVD method. Firstly, a possible limitation of CVD synthesis of N-containing diamond is the incorporation of additional, undesired defects. In particular, diamond grown by the CVD method may exhibit a brown colouration, with strong correlations observed between the N concentration in the process gases during CVD growth (necessary to produce N_S in the material) and the level of broadband-absorption features that give rise to this brown colour [37, 38]. Such features are thought to arise from vacancy chains and clusters [39–42] that are incorporated during synthesis. These defects, as well as H-related defects in CVD diamond (e.g., the nitrogen-vacancy-hydrogen defect, NVH [43]), may exhibit charge states that are paramagnetic [43, 44] and thus act as a source of dephasing, contributing to the $1/T_2^*(X)$ term in equation 3. They may also influence the value of ψ and hence influence the achieved contrast. Understanding the links between material characteristics and charge fraction, as $[N]$ is varied, is thus a key challenge. Secondly, increasing $[N]$ to the tens of ppm level in the CVD process gases has been observed to promote the formation of extended or non-epitaxial defects during growth [45, 46], thereby making it potentially challenging to achieve reproducible high- $[N]$ material with homogeneous strain [47, 48] and thus spatially-uniform and long T_2^* .

With these aims in mind, this paper therefore reports a study of N-doped CVD processes across a range of synthesis conditions (section 2), examining the resulting broadband-optical-absorption characteristics and level of charge acceptors in as-grown CVD material (section 3). Irradiated and annealed samples are then examined to assess the influences of strain and parasitic defects on key metrics relevant for NV-ensemble sensors; $[NV^-]$, ψ , and T_2^* (section 4). In section 4.2 the interplay between the as-grown charge balance (in terms of N_S) and NV^- charge-state and spin-state readout contrast are explored. Finally, based on these studies, the prospects for producing batches of samples with controlled levels of strain, $[NV]$, and T_2^* are then discussed (section 5).

2. Sample synthesis, treatment and characterisation methods

The samples examined in this paper were produced by CVD in a microwave-plasma-assisted reactor. {100}-oriented single-crystal CVD diamond plates containing $[N_S^0] \sim 0.1$ ppm acted as substrates during each deposition run. A range of synthesis conditions were utilised, in order to produce batches of samples with deliberately varying levels of $[N_S]$ and optical-absorption characteristics. This process consisted of a wide range of synthesis conditions, covering variations in substrate temperature, $T_{\text{sub}} \approx 800$ – 1100°C , N_2 concentration in the gas phase $N_{\text{gas}} \approx 10$ – 150 ppm, and methane fraction, $CH_4/H_2 \approx 1$ – 5% . CH_4 sources were used that either had natural abundances of C-isotopes, or were enriched to 99.995% ^{12}C . Synthesis was stopped once the diamond layer thickness reached ~ 1 mm in each run, in order to permit the use of multiple characterisation techniques to examine the $[N_S]$, optical absorption, and strain of the grown material.

The resulting samples were irradiated using an electron beam energy of 4.5 MeV whilst placed on a water-cooled metal bench. At this beam energy, the electron dose would be expected to be homogeneous through the thicknesses of samples grown for this paper [49]. Samples were irradiated for varying durations with the electron dose then estimated from the geometry of the system and the known current of the e^- source.

Subsequent annealing of the samples to create NV centres took place in a tube furnace with samples placed in an alumina boat. After loading, the tube was evacuated to a pressure of $\sim 1 \times 10^{-6}$ mbar in order to minimise graphitisation. Annealing was undertaken with the following thermal-ramp profile: 400°C for 2 hours, 800°C for 16 hours, 1000°C for 2 hours and 1200°C for 2 hours ($3^\circ\text{C}/\text{min}$ ramp rate), similar to the methodology employed by Chu *et al* [50].

Room-temperature optical absorption measurements to probe the absorption characteristics of samples in the range 240 – 800 nm (UV-Vis) were performed using an Analytik Jena Specord 50 Plus spectrometer. This permitted measurement of $[N_S^0]$ and estimates of the strength of absorption band features at 360 and 520 nm through spectral deconvolution and fitting of the samples post-synthesis, as described by Khan *et al* [51]. Fourier Transform Infrared spectroscopy (FTIR) spectroscopy was also used to estimate $[N_S^0]$ as well as $[N_S^+]$ in the as-grown samples, through measurement and fitting of the absorption peaks at 1130 cm^{-1} and 1344 cm^{-1} for N_S^0 and 1332 cm^{-1} for N_S^+ ; see Liggins for further details [52]. These techniques employed an aperture of 1.6 mm.

Electron Paramagnetic Resonance (EPR) at X-band frequencies (~ 9.7 GHz) was used in order to quantify the level of paramagnetic defects NVH^- , N_S^0 and NV^- in samples prior to irradiation and annealing. A sample of known $[N_S^0]$ was used as a reference and the spectral fitting and deconvolution method is described elsewhere [53, 54].

Irradiated and annealed samples were examined by low-temperature (77 K) UV-Vis absorption measurements, with samples held within an Oxford Instruments Optistat DN2 cryostat and cooled to 77 K using liquid N_2 . The integrated intensities under the

Characterisation of CVD diamond for magnetic-field sensing

8

zero-phonon-lines (ZPLs) at 575 nm and 637 nm were then used to quantify the levels of $[\text{NV}^0]$ and $[\text{NV}^-]$ respectively, using the revised calibration constants of Dale [55] (updated from those of Davies [56]). Prior to quantification of defect concentrations by the methods described, samples were exposed to UV for 2 minutes, using the Xe arc lamp excitation source of the DiamondView photoluminescence imaging instrument [37]. This is of particular importance in the case of measurements performed after annealing, since the process of heat treating a N-containing sample in the dark has been shown to reversibly alter the concentrations of point defects measured in different charge states [40]. By exposing material produced in this study to UV it was ensured that they were in a consistent state, to permit comparison between processes and samples. Measurements were conducted immediately (< 2 minutes) after exposure.

NV-based characterisation of diamond material produced in this work employed multiple experimental setups.

The first setup was designed for wide-field continuous wave optically detected magnetic resonance (CW-ODMR) imaging of mm-scale diamond samples as previously described by Kehayias *et al* [34]. From the measured CW-ODMR spectra in each pixel, both magnetic and strain-induced shifts in the NV^- spin resonances were determined by fitting to the NV^- Hamiltonian as described in previous publications [18, 34].

A second, photodiode-based setup utilised pulsed microwave control to measure the NV^- ensemble T_2^* by extracting the Ramsey free induction decay constant. Using an epi-illumination microscope configuration, 5–1000 mW of 532 nm laser light was focused through the sample with a beam-waist of 20 μm . A 2 mT applied bias magnetic field aligned with NV^- centres oriented along a single crystallographic axis to within $\sim 1^\circ$ induced a Zeeman splitting such that the $m_s = 0$ to $m_s = \pm 1$ transitions between the NV^- ground state sublevels were individually addressable with resonant MW pulses. The applied bias field homogeneity was previously engineered on this setup to ensure negligible contributions to T_2^* for the samples measured in this work [35].

Ramsey-based measurements enabled determination of T_2^* for both the single and double quantum coherences. For double quantum (DQ) Ramsey measurements (immune to axial strain-induced contributions to T_2^*), two-tone MW pulses resonant with the NV^- ground state spin transitions prepared a superposition of the $m_s = \pm 1$ states during the free precession interval. Single quantum (SQ) Ramsey measurements (sensitive to axial strain-induced contributions to T_2^*) employed single-tone MW pulses to create a superposition of the $m_s = 0$ and $m_s = +1$ or $m_s = -1$ levels during the free precession interval. See section 4.2.2 and Bauch *et al* [35] for further discussion of single and double quantum coherence measurements.

Alternatively, an additional photodiode-based, compact CW-ODMR setup was used for linewidth (γ) measurements, as a proxy for the SQ T_2^* ($T_2^*\{\text{SQ}\}$) and the relation $T_2^*\{\text{SQ}\} = 1/(\pi\gamma)$ was used in this case. Such a device was compatible with batch analysis of samples (see section 5).

Quantitative birefringence microscopy was used to assess the level of strain in samples after laser cutting and polishing of the surfaces. This was performed using

Characterisation of CVD diamond for magnetic-field sensing

9

a commercial Metripol system [57], with the methodology as discussed by Friel *et al* [48]. Images were collected through the growth face of the sample, since dislocations that thread in the growth direction are the dominant contribution to strain in CVD diamond [37, 47, 48].

3. Characterisation of as-grown material and choice of material for further study

This section describes the characterisation of samples across the range of growth conditions outlined in section 2, including their UV-Vis absorption properties, resulting colour, and concentration of $[N_S^0]$ and $[N_S^+]$. This was undertaken to ultimately produce irradiated and annealed samples with \sim ppm levels of $[NV]$ and desirable properties for B-field sensing. Samples with preferable as-grown properties are then further characterised by EPR. These initial studies were conducted with natural-abundance CH_4 gas (98.9% ^{12}C , 1.1% ^{13}C).

3.1. Characterising the nitrogen and charge environment in N-doped CVD diamond

A wide range of levels of $[N_S]$ and absorption characteristics were observed across the broad window of synthesis conditions used.

In the case of the UV-Vis absorption spectra, a peak at 270 nm was observed, which is attributed to N_S^0 [58, 59] as well as bands at 360 nm and 520 nm, which are thought to originate from clusters of vacancies and NVH^0 respectively [40]. In addition, a ramp in absorption as wavelength is decreased (of the form λ^{-3}) was present, as discussed in previous studies [40, 51]. In the case of the “type Ib” diamond component, an HPHT sample of known concentration was used and scaled appropriately to fit the spectrum and determine $[N_S^0]$. Prior to characterisation, the samples were exposed to UV, as described in section 2.

To illustrate the spread of results, the UV-Vis spectra from samples produced by two processes (P_1 and P_2) are depicted in figure 3, with the contribution from these separate components highlighted. In these example spectra the P_1 sample was found to contain $[N_S^0] = 9.5(5)$ ppm, whilst the P_2 sample had a higher concentration; $[N_S^0] = 16.2(8)$ ppm.

FTIR spectra (an example is shown in figure 4) revealed that these two samples also had dramatically varying $[N_S^+]$, with the P_1 and P_2 samples having concentrations of 10(1) ppm and 2.8(3) ppm, respectively. Hence, in the case of the sample produced by the P_1 process the levels of $[N_S^0]$ and $[N_S^+]$ are comparable. This follows the findings of previous reports of characterisation of CVD material containing > 10 ppm [60], which also measured $[N_S^0] \approx [N_S^+]$. In the case of the P_2 process sample, however, $[N_S^0] \approx 6 \times [N_S^+]$. This demonstrates that UV-Vis and/or EPR measurements solely determining $[N_S^0]$ in N-doped CVD diamond may poorly reflect the overall level of $[N]$ in this class of CVD material and that the charge balance of N_S is highly variable between different processes. In both UV-Vis and FTIR measurements an aperture of 1.6 mm was used, hence the

Characterisation of CVD diamond for magnetic-field sensing

10

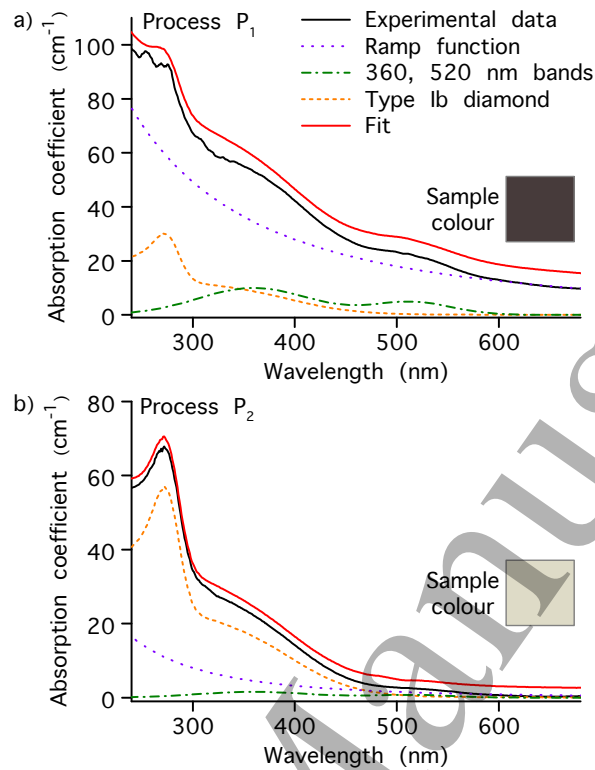


Figure 3. Representative UV-Vis absorption spectra of as-grown high-[N] CVD material, measured using a 1.6 mm aperture. (a) Material grown using CVD process P_1 , with measured $[N_S^0] = 9.5(5)$ ppm. (b) Material grown using CVD process P_2 , with measured $[N_S^0] = 16.2(8)$ ppm. In both plots, the fit has been displaced vertically for clarity and an indication of the sample colour is shown.

Table 1. Results from high-[N] diamond samples after CVD growth for two different processes (P_1 and P_2), illustrating the difference in nitrogen concentrations ($[N_S^0]$ and $[N_S^+]$) and colour of the samples as evaluated by lightness (L^*). Quoted results are averages across 5 samples in each run. Example UV-Vis absorption and FTIR spectra are shown in figure 3 and figure 4, respectively.

Process	N_S^0 (ppm)	N_S^+ (ppm)	N_S^0/N_S (χ)	L^*
P_1	9.3(5)	8(2)	0.49(8)	34(10)
P_2	17(1)	3.0(3)	0.85(1)	74(2)

quoted concentrations should be considered as being an average across this area, through the depth of the samples.

It was apparent that the colour of the two samples differed significantly (refer to figure 3). In order to assess this in a quantitative manner, images of the samples were examined in ImageJ [61] after the background was normalised to pure white, given by a lightness (L^*) value of 100 (CIELAB colour space [62]) where lightness indicates the relative brightness of a colour (an L^* value of 0 corresponds to pure black). The colour was averaged over a circular area in the centre of the samples and the L^* value for each

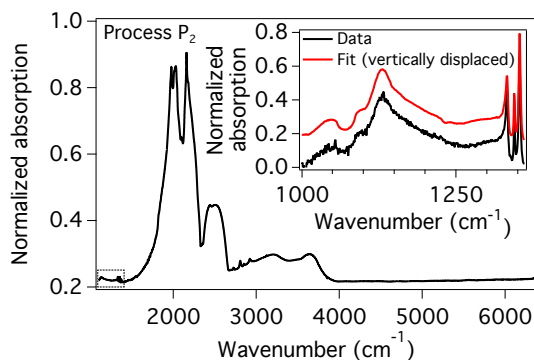


Figure 4. Representative FTIR spectrum of synthesised as-grown high-[N] CVD material for process P₂. The inset shows an enlargement of the region of the spectrum showing the 1130 cm⁻¹ and 1344 cm⁻¹ peaks (associated with N_S⁰) as well as the 1332 cm⁻¹ peak (associated with N_S⁺). The fit has been displaced vertically for clarity.

sample was determined; in this sense L* was used as a proxy for the degree of brown colouration. This, as well as the aforementioned [N_S⁰] and [N_S⁺], was then measured over a batch of five samples from both processes. The charge balance in [N_S] is defined by [N_S⁰]/[N_S] and is denoted by χ .

The results from processes P₁ and P₂ are summarised in table 1. This demonstrates that increased levels of [N_S] do not necessarily imply a degradation in absorption properties (colour) and higher fractions of [N_S⁺], related to the incorporation of parasitic defects. These factors are, instead, strongly dependent on growth conditions.

It has previously been suggested in studies by Khan *et al* that the presence of high levels of [N_S⁺] in CVD diamond may be indicative of significant brown colour [51], although limited data was provided to illustrate any such relation. Hence this trend was investigated in this current study across the entire range of explored synthesis conditions, to elucidate any correlations that may exist between the charge fraction of N_S, the colour of the samples and the absorption features present in spectra (such as those presented in figure 3). As with the P₁ and P₂ processes, 5 samples from each run were examined.

Figure 5 illustrates the data from all diamond material produced in this study. The lightness of the as-grown samples was observed to be correlated not with the determined [N_S⁰] in the samples, nor with the total [N_S] (re-enforcing the results in table 1), but with the charge fraction χ , [N_S⁰]/[N_S]. This suggests that the level of absorption leading to brown colouration is associated with the degree of acceptor-defects present in this range of [N_S].

The mapping from CVD process values such as the flow of H, CH₄ and other gases, dopant level, and substrate temperature T_{sub} onto the physical parameters controlling growth, e.g., the density of surface radical sites, the rate of CH_x addition relative to etching by H atoms, and the near-surface NH_x (or CN)/CH_x ratio, depends on the particular reactor design via intermediate variables such as the gas and electron

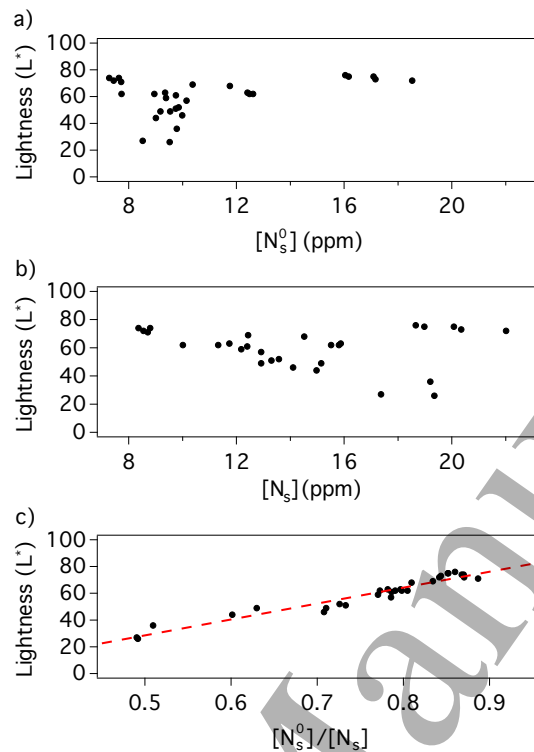


Figure 5. (a) For all material produced in this study, plot of sample lightness (evaluated as L^*) as function of neutral substitutional nitrogen concentration, $[N_S^0]$. (b) Plot constructed using the same data set as (a), but as a function of total $[N_S]$ (summing $[N_S^0]$ and $[N_S^+]$) and (c) L^* against the ratio of $[N_S^0]$ to $[N_S]$ (denoted by χ in the text). The linear fit in (c) is a guide to the eye to illustrate the link between the two parameters.

temperatures and the position of the plasma relative to the deposition area. The process conditions needed to produce given material characteristics therefore differ considerably between different reactor designs, hence it is difficult to generalise the findings in this work for other investigators in this field. Nevertheless, in this study it was established that, at a given doping level, careful simultaneous control of the CH_4 fraction (relative to total gas flow) and the substrate temperature was crucial to reducing χ whilst also maintaining a growth surface free of etch pits [63] or $\{100\}$ surface twins [64]. The incorporation of nitrogen into the solid also requires dissociation of N_2 , hence an important factor which determines the measured N_S is the rate of dissociation and the concentration of near-surface N atoms. This has not explored in this study as a function of growth conditions, but this has been the subject of previous literature [79, 80].

Further potential correlations between χ and absorption properties were investigated by examining the strength of the 520 nm and 360 nm bands (vacancy clusters and NVH^0 , respectively [40]) as a function of χ . Figure 6 illustrates the relationships observed. For both bands an increase in the absorption feature was attributed to a decrease in χ , establishing that the defects responsible for these bands

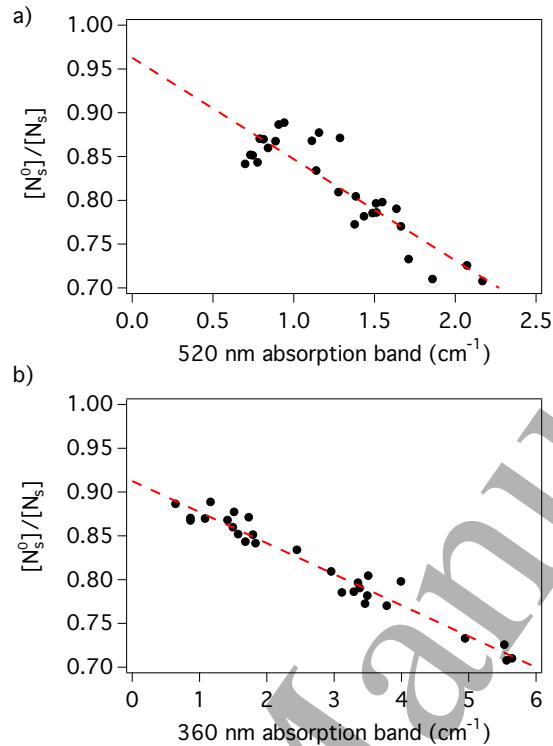


Figure 6. For all material produced in this study, relationship between the charge fraction $[N_S^0]/[N_S]$ (denoted by χ in the text) and the strength of (a) the 520 nm absorption band and (b) the 360 nm absorption band observed in an absorption spectrum measurement. Linear fit is a guide to the eye.

are acceptors. A higher spread in the results for the 520 nm band is evident (figure 6(a)), but is likely due to the relative weakness of this feature in the spectra. The examples shown in figure 3 act as a good demonstration of this behaviour, as the 360 nm and 520 nm bands are approximately a factor of three lower in figure 3(b) compared to figure 3(a), which correlates with the difference in charge-state fraction and colour of the samples, as shown in table 1. It is also noteworthy that, if a linear relationship is assumed between the N_S charge fraction and the strength of the absorption feature in both plots in figure 6, the line of best-fit trends to unity in the absence of the band. Hence, if the defects causing the 360 nm and 520 nm features were absent, negligible N_S^+ would be expected. N_S^+ is generally not observed in untreated HPHT samples and neither are these two bands.

3.2. Characterisation of process P_3 samples

Based on the findings from the samples characterised in section 3.1, a process denoted P_3 was developed, targeting $[N_S^0] \sim 15$ ppm. A small initial batch of 5 diamond samples resulted in $[N_S^0] \approx 14$ (1) ppm and $[N_S^0]/[N_S] \approx 0.81$ (2), and were utilised for further characterisation and processing.

Table 2. Summary of as-grown N-related defect concentrations in a representative sample from the high-[N] CVD process P₃ as measured by UV-Vis and FTIR absorption spectroscopy as well as electron paramagnetic resonance (EPR).

Defect	Concentration by technique (ppm)		
	UV-Vis	FTIR	EPR
N _S ⁰	13.9(7)	15(2)	16(2)
N _S ⁺		3.5(7)	
NVH ⁻			1.6(2)
NV ⁻	0.08(1)		0.070(4)

EPR measurements were conducted on a sample from this first batch, in order to investigate additional point defects present in this material. This approach allowed [NVH⁻] and [NV⁻] to be quantified in samples grown using process P₃ prior to treatment. Table 2 shows these results and summarises the quantification of [N_S⁰] by three different techniques; UV-Vis and FTIR absorption measurements, as well as EPR, in order to confirm general agreement between these methods.

The concentrations [NV⁻] and [NVH⁻] can be compared to [N_S] in order to assess the ratios of N-related defects in this material. [N_S]:[NVH⁻]:[NV⁻] in the examined sample was ~230:20:1, close to the previously observed values in studies of CVD material (300:30:1 [60] and 52:7:1 [65]). Hence, despite having high-[N] and a reduced fraction of acceptors (increased χ), NVH remains a considerable fraction of the measurable N-related defects in the studied material (>10%, given only the negative charge-state can be quantified). This likely reflects the hydrogen-rich environment that exists during the CVD growth process.

Motivated by previous reports [66–68] concerning the annealing of NV⁻ containing material at high temperatures, similar experiments were conducted on the P₃ samples. Annealing took place in vacuum at 1500°C for 16 hours to maximize any possible effects of treatments at this temperature. As shown in table 3, [NV⁻] increased to 0.2 ppm after annealing, suggesting some residual vacancy clusters were broken up in this treatment. [NV⁰] was below detection limits both before and after annealing (<0.01 ppm). A straightforward N→NV conversion is likely, echoing recent findings in treatment of layers grown on {111}-oriented substrates [68]. In the results shown in table 3, it is also notable that the 360 nm absorption band decreased dramatically in strength (by ~90%), lending support to previous assignments of V-related defects/clusters to this feature. The 520 nm feature, associated with NVH, remained unchanged, within the likely uncertainties of the measurements. Further investigation is needed to map out the extent to which vacancy related defects (especially those associated with the 360 nm band) impact NV creation and contribute to spin bath dephasing of NV⁻ ensembles [35].

Table 3. Concentrations of N_S^0 and NV^- as measured by UV-Vis and UV-Vis absorption spectra coefficients at 360 nm and 520 nm before and after sample annealing at 1500 °C for a representative sample from process P₃.

State	$[N_S^0]$ (ppm)	$[NV^-]$ (ppm)	360 nm (cm^{-1})	520 nm (cm^{-1})
As-grown	13.9(7)	0.070(4)	3.0(1)	1.5(1)
Post-anneal	13.7(7)	0.20(1)	0.3(1)	1.7(1)

4. Characterisation of material post irradiation and annealing and NV-sensing performance

This section discusses characterisation of diamond samples after electron irradiation and annealing to create \sim ppm levels of NV centres. Measurements of $[NV]$, $[NV^-]$, and $[NV^0]$ as a function of electron irradiation dose up to $6 \times 10^{18} cm^{-2}$ are presented in section 4.1. The impact of $[^{13}C]$ and strain-mitigation strategies on T_2^* are investigated in section 4.2.1 and section 4.2.2, respectively. Finally, in section 4.2.3, links between measured $[NV^-]$ and contrast and the starting material (in terms of χ) are reviewed.

4.1. Nitrogen-vacancy concentration as function of irradiation dose

To optimise the fraction of $[NV^-]$ (ψ) in the material it is crucial to choose the irradiation dose appropriately. If the irradiation dose and hence number of vacancies introduced is too low, then the generation of NV centres will be limited. Conversely, if the material is over-irradiated, $[NV]$ will be saturated as $[NV]$ approaches $N_S/2$ [65], but at the expense of generating a large number of NV^0 centres, detrimentally affecting the value of ψ [69, 70].

For the process P₃ material described in the previous section with ≈ 14 ppm $[N_S^0]$ it was therefore desirable to investigate the generation of NV^- and NV^0 centres as a function of irradiation dose. This was conducted up to a dose of $\sim 6 \times 10^{18} cm^{-2}$ and the results obtained after the samples were annealed are shown in figure 7(a). It should be noted that the samples were annealed using a ramped-temperature annealing recipe which has a final 2 hour step at 1200 °C. Although temperatures above 1000 °C do not increase $[NV]$ [27], higher temperatures have previously been shown to assist in annealing out multi-vacancy defects [71, 72]. Measurements of $[NV^-]$ and $[NV^0]$ were conducted by UV-Vis after the samples were exposed to UV.

Over this range of irradiation doses the concentration of both charge states of NV were observed to increase and $[NV]$ has not saturated ($[NV] < [N_S]/2$), however at the highest dose the ratio of $[NV^-]/[NV]$ began to decrease. This is despite N_S^0 defects remaining which could donate an electron, suggesting other defects present (potentially formed during irradiation) can act as acceptors and hence influence of the observed $[NV^-]/[NV]$. The dose was therefore not increased further and was chosen as the level of irradiation to use for the remainder of this study. At this dose, samples were found

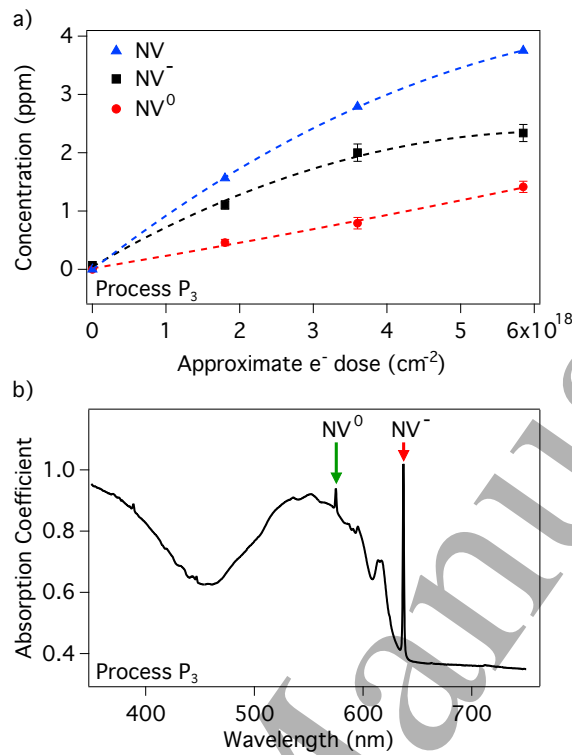


Figure 7. (a) Average concentrations of $[NV^-]$, NV^0 and $[NV]$ ($[NV^-] + [NV^0]$) of e⁻ irradiated (4.5 MeV) and annealed process P₃ samples containing ≈ 14 ppm $[N_S^0]$ as-grown, as measured by UV-Vis absorption. (b) Example 77 K UV-Vis measurement of process P₃ material after irradiation to an e⁻ dose of $\sim 6 \times 10^{18}$ cm⁻² and annealing up to 1200 °C. Measurements were made after UV exposure.

to contain 3.7 (2) ppm $[NV]$, comprising 2.3 (1) ppm of $[NV^-]$ and 1.4 (1) ppm of $[NV^0]$ after annealing and exposure to UV. An example 77 K UV-Vis absorption spectrum of this material is shown in figure 7(b).

4.2. Impact on NV Sensing Parameters

In this section the properties relevant to magnetic-field sensing of irradiated and annealed samples are reported, including T_2^* and ODMR contrast. Correlations between the final material properties and as-grown material properties (N_S charge fraction, χ) are established by comparing process P₃ to process P₁ (see section 3.1) which had a similar $[N_S]$, but a dramatically lower charge fraction due to an increased concentration of parasitic defects.

4.2.1. Influence of $[^{13}C]$ In order to initially assess irradiated and annealed material from the process P₃, as well as investigating the effect of isotopic enrichment, linewidth-based CW-ODMR measurements were performed [27].

Figures 8(a) and 8(b) show example CW-ODMR spectra for samples grown with natural abundance CH₄ (1.1% ¹³C) and ¹³C-depleted CH₄ (0.005% ¹³C), respectively.

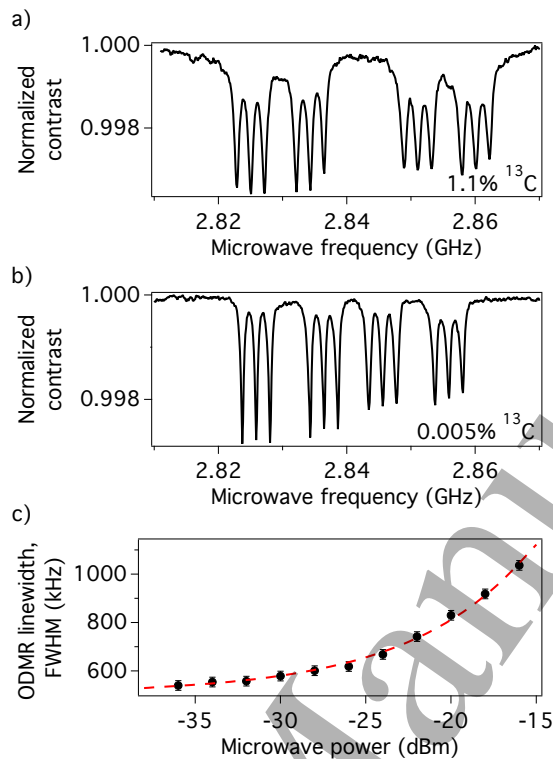


Figure 8. CW-ODMR spectra (lower-frequency half of total NV^- spectrum) of (a) 1.1% ^{13}C and (b) 0.005% ^{13}C process P_3 samples containing approximately 3.7 ppm $[\text{NV}]$. Spectra were taken in the absence of obvious microwave-power broadening. (c) FWHM of CW-ODMR spectrum shown in (b) as a function of microwave power level (subsequently passed through 30 dB amplifier).

Both samples had comparable levels of $[\text{N}_\text{S}]$ (grown by process P_3) and were treated to the same irradiation dose of $\sim 6 \times 10^{18} \text{ cm}^{-2}$. The ODMR linewidth in the limit of zero microwave power (γ) in this setup was determined to be 1000(100) kHz for the 1.1% ^{13}C sample and 510(50) kHz for the 0.005% ^{13}C sample (refer to figure 8(c)). This suggests, as expected from figure 2(a), that even at this high level of $[\text{NV}^-]$ and $[\text{N}_\text{S}^0]$, the contribution to the ensemble-NV dephasing time T_2^* of the ^{13}C term in equation 3 is still significant. Hence, an improvement in performance ($\geq 40\%$, as sensitivity scales with $\sqrt{T_2^*}$ in equation 1) can be obtained through isotopic enrichment in such samples. Growth of ^{13}C -depleted samples adds cost to the process and hence it is dependent on the end-application as to the required cost/performance balance. In this case ^{13}C -depleted samples were used in the remainder of this study as this maximises sensitivity and also assists in deconvolving the influence of other components affecting T_2^* . This effect would become more significant in future studies targeting lower concentrations of $[\text{N}]$.

4.2.2. Strain mitigation and T_2^* measurements When averaging over an ensemble of NV^- centres, strain inhomogeneity can degrade the ensemble-NV dephasing time, T_2^* ,

Characterisation of CVD diamond for magnetic-field sensing

18

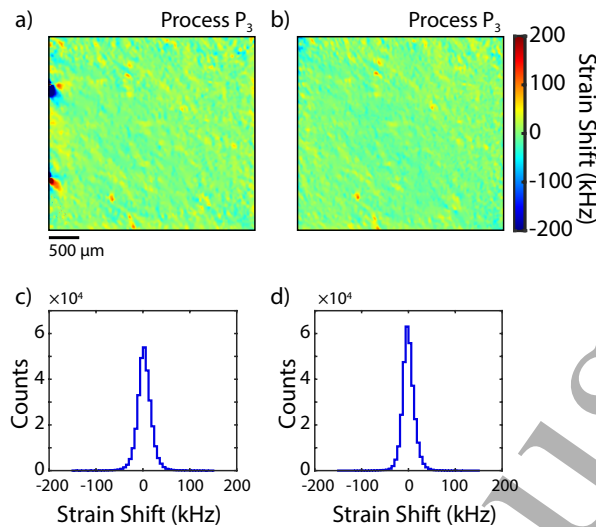


Figure 9. (a) Map of extracted strain-induced NV resonance shifts for a $(3.6 \times 3.6 \times 0.1)$ mm³ freestanding plate produced from a thicker original process P₃ sample. (b) Map of extracted strain-induced NV resonance shifts for a second freestanding plate produced from a different portion of the sample used to produce the plate shown in (a). (c,d) Histograms of the strain shift values shown in (a) and (b), respectively.

and ODMR contrast [34]. To mitigate potential strain issues CVD substrates and pre-synthesis etches were carefully controlled to minimise the density of dislocations present in the high-[N] material grown, according to the methods discussed in Friel *et al* [48]. Deposition conditions were also controlled for the duration of the run to avoid the formation of non-epitaxial crystallites.

To characterise the success of these simple strain mitigation strategies, the NV⁻ spin properties were studied. These measurements employed two 100 μm-thick freestanding plates produced from a single process P₃ sample grown with ¹³C depleted to 0.005% and subsequently irradiated and annealed. This thickness was chosen to improve the planar spatial resolution of CW-ODMR-based imaging and reduce inhomogeneities in the applied magnetic, optical, and MW control fields.

Strain-induced resonance shifts were extracted by fitting the measured CW-ODMR spectra pixel-by-pixel to the full NV Hamiltonian as described in Glenn *et al* [18] and Kehayias *et al* [34]. Due to the thickness of the diamond substrate limiting spatial resolution [18, 34], NV strain shift measurements are only advantageous for probing the strain environment for length scales larger than the thickness of the diamond, 100 μm. Maps of these shifts for the two samples are shown in figures 9(a,b) and histograms of the measured shifts are shown in figures 9(c,d), respectively. Both samples exhibit minimal strain inhomogeneity with a distribution in strain-induced shifts of approximately 25 kHz full-width half-maximum (FWHM). These measurements demonstrate lower levels strain control in these CVD process relative to previous thin-layer samples in the literature (see Kehayias *et al* [34] for typical examples of N-doped CVD diamond layers, with

strain-induced shifts on the order of hundreds of kHz to MHz). The shared spatial variations in the strain inhomogeneity between figure 9(a) and 9(b) are a consequence of the two samples being cut from the same original diamond sample (particularly visible along the bottom edges of the diamond plates).

For the sample shown in figure 9(a), additional photodiode-based Ramsey measurements of ensemble-NV T_2^* were conducted on the setup described in section 2 and previously established to have negligible contribution from B_0 gradients and temporal variations, and other technical inhomogeneities [35]. Measurements of the single and double quantum T_2^* in six different locations across the sample yielded average values of $T_2^*\{\text{DQ}\} = 0.70(5) \mu\text{s}$ and $T_2^*\{\text{SQ}\} = 1.12(6) \mu\text{s}$ where the uncertainties indicate one standard deviation.

Comparison of the single quantum T_2^* and axial-strain-immune double quantum T_2^* provides insight into the dominant dephasing sources across the interrogated ensemble, including the strain inhomogeneity on length scales shorter than the $100 \mu\text{m}$ sample thickness. As expected when limited by magnetic dipolar interactions with the surrounding spin bath, the average $T_2^*\{\text{DQ}\}$ is nearly half the average $T_2^*\{\text{SQ}\}$ due to the effectively doubled gyromagnetic ratio for the double quantum sensing basis [35]. However, the residual difference between $T_2^*\{\text{SQ}\}$ and $2 \cdot T_2^*\{\text{DQ}\}$ suggests a strain-gradient within the interrogated volume of approximately 50 kHz. This strain-induced contribution is similar to the 25 kHz distribution across the entire sample imaged in the previous section, suggesting minimal additional strain-gradients on the sub- $100 \mu\text{m}$ length-scale. The effect of strain-gradients in terms of T_2^* was also investigated in a non-strain controlled P_3 sample, with the results discussed in the supplemental material [73].

The observed $T_2^*\{\text{DQ}\}$ values are comparable to the estimated ensemble-NV dephasing, $T_2^*\{\text{DQ, est.}\} \approx 0.6 \mu\text{s}$, when dominated by dipolar interactions with residual N_S^0 bath spins and minor contributions from NV^- spins as well as NVH^- spins (estimated using table 2). For this estimate, the remaining $[N_S^0]$ in the irradiated and annealed P_3 samples was approximated by assuming the creation of each NV^0 (NV^-) consumes one (two) N_S^0 . Additionally, NV^0 and non-interrogated NV^- spins are assumed to yield a negligible contribution to the NV-ensemble dephasing. See Barry *et al*, for a detailed motivation of these assumptions [28].

Expanding on the discussion in section 1.1, the product of $[NV^-]$ and T_2^* can be used as a material figure of merit to account for the achieved density of $[NV^-]$ sensor spins. In past work [74, 75], ^{12}C -enriched (99.97%) HPHT material containing $[N_S^0]$ of $\sim 2 \text{ ppm}$ as-grown was treated to produce 0.4 ppm $[NV^-]$ and exhibited a T_2^* of $\sim 3.2 \mu\text{s}$. In such samples, the product $[NV^-] \times T_2^*$ is $1.3 \mu\text{s} \cdot \text{ppm}$, which compares to $2.7 \mu\text{s} \cdot \text{ppm}$ for the chosen material characterised in this work. The $2.7 \mu\text{s} \cdot \text{ppm}$ value also compares favourably to compiled assessments of samples in the literature [27, 28, 76].

4.2.3. NV charge-state and contrast Sections 3.1 and 3.2 focused on maximising the value of $[N_S^0]/[N_S]$ (χ), i.e., minimising charge traps, in as-grown material with the

Table 4. Results obtained from material made by processes P_1 and P_3 , which have similar starting levels of $[N_S]$, but different fractions $[N_S^0]/[N_S]$. Process P_3 was the chosen process for samples reviewed in section 3.1–3.2. Concentrations were determined after exposure to UV. Uncertainties indicate one standard deviation across three samples for each process.

Process	As-grown		Post irradiation and annealing	
	$[N_S]$ (ppm)	$[N_S^0]/[N_S]$ (χ)	$[NV]$ (ppm)	$[NV^-]/[NV]$ (ψ)
P_1	17(1)	0.49(8)	3.6(1)	0.43(7)
P_3	16(2)	0.81(2)	3.8(2)	0.62(5)

rationale that this would be beneficial to improve the NV charge ratio ψ . Hence, it is worthwhile to examine whether the material produced in this study can elucidate the relationship between the concentration of charge-traps in as-grown CVD material and the values of ψ (and ODMR contrast) after irradiation and annealing.

To demonstrate an understanding and control of charge trap synthesis, a charge-state-detrimental process (process P_1) was used that produced $[N_S]=17(1)$ ppm with $\chi = 0.49(8)$, compared to $[N_S]=16(2)$ ppm with $\chi = 0.81(2)$ in process P_3 . Hence, in this case, the two processes had similar $[N_S]$, but with significantly different levels of acceptors. As expected, the material also had visibly different absorption properties (section 3.1) post growth. The degree of variation in N_S charge fraction χ was also larger in the case of diamond material with lower χ , implying this process was less controlled.

Three samples grown using process P_1 were irradiated to the same dose as that used for process P_3 (section 4.1) and were annealed utilising an equivalent thermal profile. The results obtained from these processes are shown in table 4. The NV charge fraction ψ is reduced in the process P_1 sample, suggesting that grown-in defects in CVD diamond that act as charge acceptors can have a detrimental influence on the yield of $[NV^-]$.

The optical-absorption properties of material grown by these two processes were also investigated. It was found that the P_1 material, with a higher starting level of brown colouration (lower χ), still had a higher level of absorption post irradiation and annealing (around 10–15% higher in the range 350–550 nm). Increasing $[NV]$, whilst limiting absorption from other defects at wavelengths < 637 nm, is beneficial from the perspective of reducing absorption from the laser used to excite NV-luminescence. Hence a material with a higher starting χ is desirable.

ODMR contrast, which depends upon the NV charge fraction under excitation and scales inverse-linearly with magnetic sensitivity, is another critical material-based factor to optimise [26–28]. The ODMR contrast for material produced using processes P_1 and P_3 was compared using pulsed-ODMR, as depicted in figure 10(a). Measurements were performed as a function of excitation intensity to account for changes in charge state under 532 nm illumination and T_1 -related effects. The ODMR contrast measurements shown in figure 10(b) indicate the maximum observed contrast during the optical pulse. A pinhole was introduced to the NV fluorescence collection path of the setup used

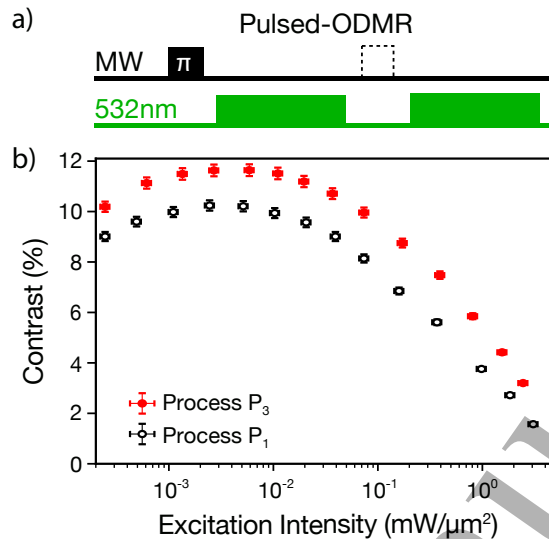


Figure 10. NV pulsed-ODMR contrast measurements of samples grown with processes P₁ and P₃. (a) Schematic of the sequence used to measure the NV contrast. Before the first 532 nm optical pulse (green), a resonant microwave (MW) pulse is applied to transfer population from the $m_s = 0$ to the $m_s = 1$ state. The black dashed pulse indicates that no MW pulse was applied before the second optical pulse. Optical pulses are 5 ms in duration and not shown to scale. (b) ODMR contrast as a function of excitation intensity for 100 μm -thick samples produced using process P₁ and P₃. The reported contrast was determined by the maximum ratio between $n_{\text{sig}}/n_{\text{ref}}$ during a readout pulse of 532 nm laser light where n_{sig} (n_{ref}) corresponds to the fluorescence measured with (without) an applied MW π -pulse. Horizontal error bars indicate an estimated 10% uncertainty in the measured intensity and vertical error bars indicate an estimated 2% uncertainty in measured contrast.

in section 4.2.2 to restrict the collection volume and ensure homogeneous illumination similar to the approach in Alsid *et al* [30]. The fixed 5 ms optical pulse duration was sufficient to achieve a steady-state fluorescence for all excitation intensities.

Since NV-ensemble devices commonly employ a long-pass filter to partially isolate NV⁻ photo-luminescence (PL) from background NV⁰ PL [30, 31], a 647 nm long-pass filter was added to replicate realistic experimental conditions. As shown in figure 10(b), the measured pulsed-ODMR for process P₃ exceeds that of process P₁ by approximately 20% across a range of 532 nm excitation intensities spanning from near saturation intensity around $1\text{--}3 \text{ mW}/\mu\text{m}^2$ [28] (optimal for applications using pulsed measurement protocols) down to $10^{-4} \text{ mW}/\mu\text{m}^2$ (similar to the intensities used for CW-ODMR applications [77]). The two samples exhibit maximum contrast for excitation intensities around $5 \times 10^{-3} \text{ mW}/\mu\text{m}^2$ with values of 12% and 10% for processes P₃ and P₁, respectively. At higher intensities, the measured contrast decreases for both samples, likely due to reduced NV charge fraction $[\text{NV}^-]/[\text{NV}]$ with increasing optical intensity [30, 31]. At lower excitation intensities, the measured contrast also decreases because the fraction of NV⁻ centres initialised into the $m_s = 0$ state depends upon the ratio of the optical pumping rate to the depolarisation rate $1/T_1$ (see the Appendix of Dréau *et*

Characterisation of CVD diamond for magnetic-field sensing

22

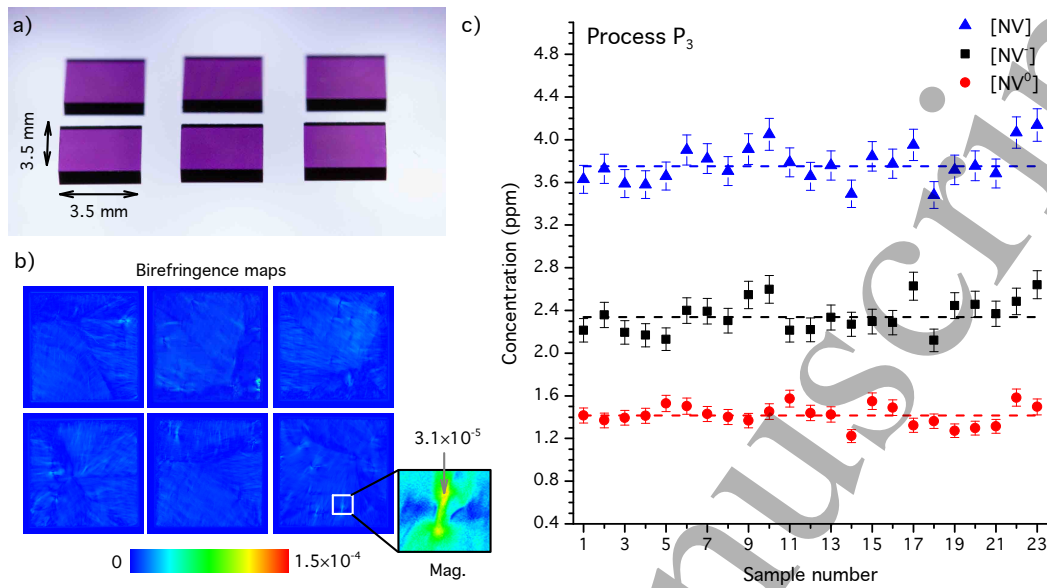


Figure 11. (a) Photograph of 6 process P₃ samples (0.005% ¹³C) with approximately 900 μm thickness, after irradiation and annealing to create ≈ 3.8 ppm [NV]. (b) Birefringence images of the plates in (a) as measured on a Metripol microscope. (c) Concentration results, determined by UV-Vis absorption, of [NV⁰], [NV⁻] and total [NV] (sum of [NV⁰] and [NV⁻]) across a batch of 23 process P₃ samples.

al for further details [78]).

The largest measured pulsed-ODMR contrasts for both processes, 10% and 12% respectively, are favourable compared to the maximum contrast attainable for NV⁻ ensembles. Assuming a typical single NV⁻ contrast of 30%, an ensemble with NV⁻ centres along all four crystal axes has a maximum possible conventional optical readout contrast of 15% when the excitation laser polarisation optimally addresses two of the four orientations (as done in this present work). Experimentally, the observed contrast is typically less than 15% because the NV⁻ PL cannot be completely isolated from the NV⁰ PL background due to the broad, overlapping phonon sidebands at room temperature [30, 31].

The pulsed-ODMR measurements on plates produced using processes P₁ and P₃ therefore imply that as-grown defects in CVD diamond that act as acceptors may impact the material properties after irradiation and annealing. The improvement in NV charge fraction, ψ , for the P₃ process simultaneously offers higher contrast across a broad range of optical excitation intensities and increased [NV⁻]. However, while beneficial for magnetic sensitivity, the observed increase in ODMR contrast between processes P₁ and P₃ is modest compared to the difference in NV charge fraction (refer to table 4) for two reasons: (a) the detected PL is predominately from NV⁻ due to the 647 nm long-pass filter which partially isolates the NV⁻ PL from NV⁰ PL and simulates realistic sensing conditions and (b) the conversion of NV⁻ to NV⁰ is less detrimental to optical contrast than may be expected because the NV⁻ charge state has a $\sim 2 \times$ higher level

of PL compared to NV^0 under weak 532 nm illumination [30].

Further work is required to understand how the maximum achievable NV charge fraction, ψ , scales with reduced levels of $[N_S]$, where the relative concentration of residual donors/acceptors are likely to be significantly altered. Nevertheless, the increased level of contrast and moderate reduction in absorption in this study suggests value in evaluating as-grown material in terms of its N_S charge fraction, χ , during the development of synthesis processes.

5. Batch analysis of samples

In this section, batch characterisation of samples is reported to demonstrate the potential for reproducible production of material with well-controlled $[NV^-]$ and ODMR linewidth (proxy to T_2^*). As-grown ^{13}C -depleted (0.005% ^{13}C) samples grown by the P_3 process were irradiated and annealed using the selected dose of $6 \times 10^{18} \text{ cm}^{-2}$ identified previously in section 4.1. Examples of these samples, post irradiation and annealing, are shown in figure 11(a). The intense purple colour is a result of the high $[NV^-]$ achieved in this material. Across such a batch of 23 samples produced in the same synthesis run, the average $[N_S^0]$ was ≈ 13 ppm with a standard deviation of 1 ppm, which demonstrates the ability to achieve the same level of $[N_S^0]$ in a larger batch, as well as repeatability between separate synthesis runs (refer to table 2 and table 3 for measurements of $[N_S^0]$ in other runs). As shown in figure 11(c), the measured $[NV] = 3.8(2)$ ppm ($[NV^-] = 2.3(2)$ ppm) was similarly consistent across the batch and with previous samples grown using process P_3 (section 4.1). The measured $[NV^-]$ and $[NV^0]$ yield a favourable average charge fraction of $\psi = 0.62(5)$ (uncertainty indicates one standard deviation).

The strain environment of each sample was characterised using Metripol birefringence imaging and representative images are shown in figure 11(b). In these samples, an average birefringence $\Delta n \approx 7(1) \times 10^{-6}$ was determined with peak values of $\Delta n \sim 3 \times 10^{-5}$ in isolated petal features (see inset of figure 11(b) for an example). A vast majority (>99%) of the pixel values within the birefringence image, figure 11(b), satisfy $\Delta n \lesssim 10^{-5}$, the standard for ultra-low birefringence diamond established by Friel *et al* [48]. The material characterised in the previous section had equivalent levels of birefringence, hence the achieved low level of strain-induced NV shift appears to be achievable in batches of samples without additional measures being required.

Comparison of Ramsey-based measurements on P_3 samples in section 4.2.2 and the linewidth (LW)-based measurements reported in section 4.2.1 enables a B-field inhomogeneity contribution for the compact CW-ODMR setup to be estimated according to the relation:

$$\frac{1}{T_2^* \{\Delta B_0\}} = \frac{1}{T_2^* \{\text{LW}\}} - \frac{1}{2 \times T_2^* \{\text{DQ}\}} \quad (5)$$

Equation 5 yields a value for $1/T_2^* \{\Delta B_0\} \sim 0.7 \mu\text{s}^{-1}$ when estimated using measurements of either the natural-abundance or ^{13}C -depleted material. In combination with the known contribution of 1.1% ^{13}C to dephasing, this estimate for the B-field

contribution enables the Ramsey T_2^* of a ^{13}C -depleted sample to be inferred using a simple and inexpensive, linewidth-based method.

Across the batch of 23 samples $\gamma = 480(30)$ kHz was determined, hence the measured linewidth varied by less than 10% between samples. Correcting for the estimated B_0 inhomogeneity in this setup (equation 5) results in a T_2^* of $\sim 1.2 \mu\text{s}$, as was expected for this material in the absence of strain. Hence the favourable properties of $[\text{NV}^-]$ and T_2^* appear to be extendable to batches of CVD samples.

6. Conclusion

This study illustrates the wide range of diamond material, in terms of absorption characteristics and relative concentrations of N_S^0 and N_S^+ , that may be produced with N-doped CVD processes. In the range 10–20 ppm strong relationships are observed between the colour of the samples and the $[\text{N}_\text{S}^0]/[\text{N}_\text{S}]$ charge fraction χ , which is related to the incorporation of unwanted, vacancy-related defects in such samples. However, it is determined that high values of χ can be achieved independent of $[\text{N}_\text{S}]$ up to 20 ppm, hence this does not represent a major concern for production of such material by CVD.

Comparison of material grown with the same initial $[\text{N}_\text{S}]$ before and after irradiation and annealing suggests that improved χ in as-grown material increases $\text{N}_\text{S} \rightarrow \text{NV}^-$ conversion, thereby increasing the density of NV^- sensor spins and ODMR measurement contrast, which both benefit sensing applications.

The correlation of the desired material properties, such as $[\text{NV}^-]$ after irradiation and annealing, with simple CVD-growth metrics, such as the colour of as-grown samples, enables rapid exploration of large synthesis parameter spaces. This approach provides an efficient framework to develop future diamond material with varying defect densities tailored to specific applications.

This study also demonstrates that ensemble-NV-diamond samples with controlled levels of strain and reproducible $[\text{NV}^-]$ and T_2^* may be produced by CVD, shown through characterisation of 23 near-identical samples. The NV^- concentration was observed to vary by less than 7% with an average of 2.3(2) ppm as measured by UV-Vis absorption spectroscopy. Furthermore, birefringence, CW-ODMR strain-imaging, and Ramsey-based T_2^* measurements suggest that careful substrate surface preparation and pre-synthesis etches is sufficient to control strain inhomogeneity in the material to largely mitigate strain-gradient-induced contributions to ensemble-NV dephasing. These findings are positive for the academic and industrial efforts focused on the production, by the CVD method, of reproducible high- $[\text{NV}]$ material with favourable properties for magnetic-field sensing.

Material presented in this study would be expected to provide sensitivity improvements for current NV-ensemble devices, without the additional experimental complexity or power consumption associated with advanced spin control or readout techniques [28]. CVD processes producing diamond with this range of $[\text{N}_\text{S}]$ therefore appears to be an area that deserves further study. This is especially true in the case of

production of micron-scale, NV-rich surface layers of such material, as this would enable advances in NV-ensemble wide-field magnetic imaging applications. For such growths, control of additional qualities such as surface morphology and a well-defined interface between the high-purity diamond substrate and N-doped layer will be critical.

Acknowledgements

The authors acknowledge Rajesh Patel and Gavin Morley (University of Warwick) for performing the EPR measurements on the as-grown sample examined in table 2. This material is based upon work supported by, or in part by, the U.S. Army Research Laboratory and the U.S. Army Research Office under Grant No. W911NF-15-1-0548; the National Science Foundation (NSF) Physics of Living Systems (PoLS) program under Grant No. PHY-1504610; the Air Force Office of Scientific Research Award No. FA9550-17-1-0371; the Defense Advanced Research Projects Agency Driven and Nonequilibrium Quantum Systems (DARPA DRINQS) program under Award No. D18AC00033; the Department of Energy (DOE) Quantum Information Science Enabled Discovery (QuantISED) program under Award No. DE-SC0019396; and Lockheed Martin under Contract No. A32198. Element Six also acknowledges support from the ASTERIQS program, Grant No. 820394, of the European Commission.

References

- [1] Doherty M W, Manson N B, Delaney P, Jelezko F, Wrachtrup J and Hollenberg L C L 2013 *Phys. Rep.* **528** 1–45
- [2] Balasubramanian G, Neumann P, Twitchen D, Markham M, Kolesov R, Mizuochi N, Isoya J, Achard J, Beck J, Tissler J, Jacques V, Hemmer P R, Jelezko F and Wrachtrup J 2009 *Nat. Mater.* **8** 383–7
- [3] Stanwix P L, Pham L M, Maze J R, Le Sage D, Yeung T K, Cappellaro P, Hemmer P R, Yacoby A, Lukin M D and Walsworth R L 2010 *Phys. Rev. B* **82** 201201
- [4] Jelezko F and Wrachtrup J 2006 *Phys. Status Solidi A* **203** 3207–25
- [5] Taylor J M, Cappellaro P, Childress L, Jiang L, Budker D, Hemmer P R, Yacoby A, Walsworth R and Lukin M D 2008 *Nat. Phys.* **4** 810–6
- [6] Degen C L 2008 *Appl. Phys. Lett.* **92** 243111
- [7] Acosta V M, Bauch E, Ledbetter M P, Waxman A, Bouchard L S and Budker D 2010 *Phys. Rev. Lett.* **104** 070801
- [8] Rondin L, Tetienne J P, Hingant T, Roch J F, Maletinsky P and Jacques V 2014 *Rep. Prog. Phys.* **77** 056503
- [9] Isberg J, Hammersberg J, Johansson E, Wikstrom T, Twitchen D J, Whitehead A J, Coe S E and Scarsbrook G A 2002 *Science* **297** 1670–2
- [10] Gibney E 2014 *Nature* **505** 472–4
- [11] Wolf T, Neumann P, Nakamura K, Sumiya H, Ohshima T, Isoya J and Wrachtrup J 2015 *Phys. Rev. X* **5** 041001
- [12] Maertz B J, Wijnheijmer A P, Fuchs G D, Nowakowski M E and Awschalom D D 2010 *Appl. Phys. Lett.* **96** 092504
- [13] Pham L M, Sage D L, Stanwix P L, Yeung T K, Glenn D, Trifonov A, Cappellaro P, Hemmer P R, Lukin M D, Park H, Yacoby A and Walsworth R L 2011 *New J. Phys.* **13** 045021

Characterisation of CVD diamond for magnetic-field sensing 26

- [14] Le Sage D, Arai K, Glenn D R, DeVience S J, Pham L M, Rahn-Lee L, Lukin M D, Yacoby A, Komeili A and Walsworth R L 2013 *Nature* **496** 486
- [15] Glenn D R, Lee K, Park H, Weissleder R, Yacoby A, Lukin M D, Lee H, Walsworth R L and Connolly C B 2015 *Nat. Methods* **12** 736
- [16] Shao L, Liu R, Zhang M, Shneidman A V, Audier X, Markham M, Dhillon H, Twitchen D J, Xiao Y F and Lončar M 2016 *Adv. Opt. Mater.* **4** 1075–80
- [17] Tetienne J P, Dontschuk N, Broadway D A, Stacey A, Simpson D A and Hollenberg L C L 2017 *Sci. Adv.* **3** e1602429
- [18] Glenn D R, Fu R R, Kehayias P, Le Sage D, Lima E A, Weiss B P and Walsworth R L 2017 *Geochem., Geophys., Geosyst.* **18** 3254–67
- [19] Simpson D A, Tetienne J P, McCoe J M, Ganesan K, Hall L T, Petrou S, Scholten R E and Hollenberg L C L 2016 *Sci. Rep.* **6** 22797
- [20] Ku M J H, Zhou T X, Li Q, Shin Y J, Shi J K, Burch C, Zhang H, Casola F, Taniguchi T, Watanabe K, Kim P, Yacoby A and Walsworth R L Imaging Viscous Flow of the Dirac Fluid in Graphene Using a Quantum Spin Magnetometer (*Preprint* 1905.10791)
- [21] Nowodzinski A, Chipaux M, Toraille L, Jacques V, Roch J F and Debuisschert T 2015 *Microelectron. Reliab.* **55** 1549–53
- [22] Turner M J, Langellier N, Bainbridge R, Walters D, Meesala S, Babinec T M, Kehayias P, Yacoby A, Hu E, Lončar M, Walsworth R L and Levine E V 2020 Magnetic field fingerprinting of integrated circuit activity with a quantum diamond microscope (*Preprint* 2004.03707)
- [23] Chipaux M, Toraille L, Larat C, Morvan L, Pezzagna S, Meijer J and Debuisschert T 2015 *Appl. Phys. Lett.* **107** 233502
- [24] Canciani A and Raquet J 2016 *Navigation* **63** 111–26
- [25] Sheinker A, Frumkis L, Ginzburg B, Salomonski N and Kaplan B Z 2009 *IEEE Trans. Magn.* **45** 160–7
- [26] Budker D and Romalis M 2007 *Nat. Phys.* **3** 227–34
- [27] Acosta V M, Bauch E, Ledbetter M P, Santori C, Fu K M C, Barclay P E, Beausoleil R G, Linget H, Roch J F, Treussart F, Chemerisov S, Gawlik W and Budker D 2009 *Phys. Rev. B* **80** 115202
- [28] Barry J F, Schloss J M, Bauch E, Turner M J, Hart C A, Pham L M and Walsworth R L 2020 *Rev. Mod. Phys.* **92**(1) 015004
- [29] Davies G, Lawson S C, Collins A T, Mainwood A and Sharp S J 1992 *Phys. Rev. B* **46** 13157
- [30] Alsid S T, Barry J F, Pham L M, Schloss J M, O’Keeffe M F, Cappellaro P and Braje D A 2019 *Phys. Rev. Appl.* **12**(4) 044003
- [31] Aude Craik D P L, Kehayias P, Greenspon A S, Zhang X, Turner M J, Schloss J M, Bauch E, Hart C A, Hu E L and Walsworth R L A microwave-assisted spectroscopy technique for determining charge state in nitrogen-vacancy ensembles in diamond (*Preprint* 1811.01972)
- [32] Lawson S C, Fisher D, Hunt D C and Newton M E 1998 *J. Phys. Condens. Mat.* **10** 6171–80
- [33] Dolde F, Fedder H, Doherty M W, Nöbauer T, Rempp F, Balasubramanian G, Wolf T, Reinhard F, Hollenberg L C L, Jelezko F and Wrachtrup J 2011 *Nat. Phys.* **7** 459–63
- [34] Kehayias P, Turner M J, Trubko R, Schloss J M, Hart C A, Wesson M, Glenn D R and Walsworth R L 2019 *Phys. Rev. B* **100** 174103
- [35] Bauch E, Hart C A, Schloss J M, Turner M J, Barry J F, Kehayias P, Singh S and Walsworth R L 2018 *Phys. Rev. X* **8** 031025
- [36] Burns R C, Cvetkovic V, Dodge C N, Evans D J F, Rooney M L T, Spear P M and Welbourn C M 1990 *J. Cryst. Growth* **104** 257–79
- [37] Martineau P M, Lawson S C, Taylor A J, Quinn S J, Evans D J F and Crowder M J 2004 *Gems Gemol.* **40** 2–25
- [38] Tallaire A, Mayer L, Brinza O, Pinault-Thaury M A, Debuisschert T and Achard J 2017 *Appl. Phys. Lett.* **111** 143101
- [39] Khan R, Martineau P, Cann B, Newton M, Dhillon H and Twitchen D 2010 *Gems Gemol.* **46** 18–26

- 1
2
3 *Characterisation of CVD diamond for magnetic-field sensing* 27
4
5 [40] Khan R U A, Martineau P M, Cann B L, Newton M E and Twitchen D J 2009 *J. Phys.: Condens.*
6 *Matter* **21** 364214
7 [41] Hounscome L S, Jones R, Martineau P M, Fisher D, Shaw M J, Briddon P R and Öberg S 2006
8 *Phys. Rev. B* **73** 125203
9 [42] Fujita N, Jones R, Öberg S and Briddon P R 2009 *Diamond Relat. Mater.* **18** 843–5
10 [43] Glover C, Newton M E, Martineau P, Twitchen D J and Baker J M 2003 *Phys. Rev. Lett.* **90**
11 185507
12 [44] Glover C, Newton M E, Martineau P M, Quinn S and Twitchen D J 2004 *Phys. Rev. Lett.* **92**
13 135502
14 [45] Willems B, Tallaire A and Achard J 2014 *Diamond Relat. Mater.* **41** 25–33
15 [46] Tallaire A, Achard J, Silva F, Brinza O and Gicquel A 2013 *C. R. Phys.* **14** 169–84
16 [47] Gaukroger M, Martineau P, Crowder M, Friel I, Williams S and Twitchen D 2008 *Diamond Relat.*
17 *Mater.* **17** 262–9
18 [48] Friel I, Clewes S L, Dhillon H K, Perkins N, Twitchen D J and Scarsbrook G A 2009 *Diamond*
19 *Relat. Mater.* **18** 808–15
20 [49] Campbell B, Choudhury W, Mainwood A, Newton M and Davies G 2002 *Nucl. Instrum. Methods*
21 *Phys. Res., Sect. A* **476** 680–5
22 [50] Chu Y, de Leon N P, Shields B J, Hausmann B, Evans R, Togan E, Burek M J, Markham M,
23 Stacey A, Zibrov A S, Yacoby A, Twitchen D J, Loncar M, Park H, Maletinsky P and Lukin
24 M D 2014 *Nano Lett.* **14** 1982–6
25 [51] Khan R U A, Cann B L, Martineau P M, Samartseva J, Freeth J J P, Sibley S J, Hartland C B,
26 Newton M E, Dhillon H K and Twitchen D J 2013 *J. Phys.: Condens. Matter* **25** 275801
27 [52] Liggins S 2010 *Identification of point defects in treated single crystal diamond* PhD Thesis University
28 of Warwick URL <http://wrap.warwick.ac.uk/35522/>
29 [53] Edmonds A M 2008 *Magnetic resonance studies of point defects in single crystal diamond* PhD
30 Thesis University of Warwick URL <http://wrap.warwick.ac.uk/2968>
31 [54] Tallaire A, Collins A T, Charles D, Achard J, Sussmann R, Gicquel A, Newton M E, Edmonds
32 A M and Cruddace R J 2006 *Diamond Relat. Mater.* **15** 1700–7
33 [55] Dale M W 2015 *Colour Centres on Demand in Diamond* PhD Thesis University of Warwick URL
34 <http://wrap.warwick.ac.uk/80044/>
35 [56] Davies G 1999 *Physica B Condens. Matter* **273-274** 15–23
36 [57] Glazer A M, Lewis J G and Kaminsky W 1996 *Proc. R. Soc. London, Ser. A* **452** 2751–65
37 [58] Dyer H B, Raal F A, Preez L D and Loubser J H N 1965 *Philos. Mag.* **11** 763–74
38 [59] Chrenko R M, Strong H M and Tuft R E 1971 *Philos. Mag.* **23** 313–8
39 [60] Edmonds A M, D’Haenens-Johansson U F S, Cruddace R J, Newton M E, Fu K M C, Santori C,
40 Beausoleil R G, Twitchen D J and Markham M L 2012 *Phys. Rev. B* **86** 035201
41 [61] Schneider C A, Rasband W S and Eliceiri K W 2012 *Nat. Methods* **9** 671–5
42 [62] McLaren K 1976 *J. Soc. Dyers Colour.* **92** 338–41
43 [63] Achard J, Tallaire A, Sussmann R, Silva F and Gicquel A 2005 *J. Cryst. Growth* **284** 396–405
44 [64] Wild C, Kohl R, Herres N, Muller-Sebert W and Koidl P 1994 *Diamond Relat. Mater.* **3** 373–81
45 [65] Hartland C 2014 *A study of point defects in CVD diamond using electron param-*
46 *agnetic resonance and optical spectroscopy* PhD Thesis University of Warwick URL
47 <http://wrap.warwick.ac.uk/67156>
48 [66] Orwa J O, Santori C, Fu K M C, Gibson B, Simpson D, Aharonovich I, Stacey A, Cimmino A,
49 Balog P, Markham M, Twitchen D, Greentree A D, Beausoleil R G and Prawer S 2011 *J. Appl.*
50 *Phys.* **109** 083530
51 [67] Tetienne J P, de Gille R W, Broadway D A, Teraji T, Lillie S E, McCoey J M, Dontschuk N, Hall
52 L T, Stacey A, Simpson D A and Hollenberg L C L 2018 *Phys. Rev. B* **97** 085402
53 [68] Osterkamp C, Mangold M, Lang J, Balasubramanian P, Teraji T, Naydenov B and Jelezko F 2019
54 *Sci. Rep.* **9** 5786
55 [69] Mita Y 1996 *Phys. Rev. B* **53** 11360–4
56
57
58
59
60

1
2
3 *Characterisation of CVD diamond for magnetic-field sensing* 28
4

- 5 [70] Waldermann F, Olivero P, Nunn J, Surmacz K, Wang Z, Jaksch D, Taylor R, Walmsley I, Draganski
6 M, Reichart P, Greentree A, Jamieson D and Prawer S 2007 *Diamond Relat. Mater.* **16** 1887–95
7 [71] Naydenov B, Reinhard F, Lämmle A, Richter V, Kalish R, D’Haenens-Johansson U F S, Newton
8 M, Jelezko F and Wrachtrup J 2010 *Appl. Phys. Lett.* **97** 242511
9 [72] Yamamoto T, Umeda T, Watanabe K, Onoda S, Markham M L, Twitchen D J, Naydenov B,
10 McGuinness L P, Teraji T, Koizumi S, Dolde F, Fedder H, Honert J, Wrachtrup J, Ohshima T,
11 Jelezko F and Isoya J 2013 *Phys. Rev. B* **88** 075206
12 [73] Additional details are included in the supplemental material.
13 [74] Stürner F M, Brenneis A, Kassel J, Wostradowski U, Rölver R, Fuchs T, Nakamura K, Sumiya H,
14 Onoda S, Isoya J and Jelezko F 2019 *Diamond Relat. Mater.* **93** 59–65
15 [75] Grezes C, Julsgaard B, Kubo Y, Ma W L, Stern M, Bienfait A, Nakamura K, Isoya J, Onoda S,
16 Ohshima T, Jacques V, Vion D, Esteve D, Liu R B, Mølmer K and Bertet P 2015 *Phys. Rev.*
17 *A* **92** 020301
18 [76] Nöbauer T, Buczak K, Angerer A, Putz S, Steinhauser G, Akbarzadeh J, Peterlik H, Majer J,
19 Schmiedmayer J and Trupke M Creation of ensembles of nitrogen-vacancy centers in diamond
20 by neutron and electron irradiation (*Preprint* 1309.0453)
21 [77] Levine E V, Turner M J, Kehayias P, Hart C A, Langellier N, Trubko R, Glenn D R, Fu R R and
22 Walsworth R L 2019 *Nanophotonics* **8** 1945
23 [78] Dréau A, Lesik M, Rondin L, Spinicelli P, Arcizet O, Roch J F and Jacques V 2011 *Phys. Rev. B*
24 **84** 195204
25 [79] Truscott B S, Kelly M W, Potter K J, Johnson M and Ashfold M N R 2015 *J. Phys. Chem. A*
26 **119** 12962–76
27 [80] Truscott B S, Kelly M W, Potter K J, Ashfold M N R and Mankelevich Y A 2016 *J. Phys. Chem.*
28 *A* **120** 8537–49
29
30
31
32
33
34
35
36
37
38
39
40
41
42
43
44
45
46
47
48
49
50
51
52
53
54
55
56
57
58
59
60